CrossMark

J. Fluid Mech. (2020), *vol*. 903, A39. © The Author(s), 2020.
Published by Cambridge University Press
doi:10.1017/jfm.2020.623

Regime crossover in Rayleigh–Bénard convection with mixed boundary conditions

Rodolfo Ostilla-Mónico[1],† **and Amit Amritkar**[1,2]

[1]Department of Mechanical Engineering, University of Houston, Houston, TX 77204, USA
[2]HPE Data Science Institute, University of Houston, Houston, TX 77204, USA

(Received 13 January 2020; revised 4 June 2020; accepted 21 July 2020)

We numerically simulate three-dimensional Rayleigh–Bénard convection, the flow in a fluid layer heated from below and cooled from above, with inhomogeneous temperature boundary conditions, to explore two distinct regimes described in recent literature. We fix the non-dimensional temperature difference, i.e. the Rayleigh number, to $Ra = 10^8$, and vary the Prandtl number between 1 and 100. By introducing stripes of adiabatic boundary conditions on the top plate, and making the surface of the top plate only 50 % conducting, we modify the heat transfer, the average temperature profiles and the underlying flow properties. We find two regimes: when the pattern wavelength is small, the flow is barely affected by the stripes. The heat transfer is reduced, but remains a large fraction of that of the unmodified case, and the underlying flow is only slightly modified. When the pattern wavelength is large, the heat transfer saturates to approximately two-thirds of the value of the unmodified problem, the temperature in the bulk increases substantially, and velocity fluctuations in the directions normal to the stripes are enhanced. The transition between the two regimes happens at pattern wavelength around the distance between the two plates, with different quantities transitioning at slightly different wavelength values. This transition is approximately Prandtl-number-independent, even if the statistics in the long-wavelength regime slightly vary.

Key words: Bénard convection, mantle convection, turbulent convection

1. Introduction

Rayleigh–Bénard (RB) convection, the flow in a layer heated from below and cooled from above, is a canonical model for the problem of thermal convection (Ahlers, Grossmann & Lohse 2009; Lohse & Xia 2010; Chillà & Schumacher 2012). The study of RB convection has proven so fruitful because the system is well-defined and closed and possesses non-trivial conservation properties accessible to theory and experiment, such as the exact relationship between kinetic energy dissipation and heat transport (Shraiman & Siggia 1990). However, most real systems, both in process technology and in nature, differ from the idealized RB set-up. Many modifications of the canonical system are possible, such as the addition of roughness (Tisserand *et al.* 2011; Rusaouën *et al.* 2018), finite conductivity effects on the plates (Verzicco 2004; Brown *et al.* 2005) or different sidewall conditions (Xia & Lui 1997; van der Poel *et al.* 2014). A variation which has attracted

† Email address for correspondence: rostilla@central.uh.edu

https://doi.org/10.1017/jfm.2020.623 Published online by Cambridge University Press

recent attention is that of inhomogeneous temperature boundary conditions, which is of interest in geophysics (Pekeris 1935; Solomatov & Moresi 2000; Lenardic & Moresi 2003; Lenardic *et al.* 2005). To model the difference between continental and oceanic lithospheres, studies have substituted the constant-temperature top boundary condition by a pattern of adiabatic and conducting boundary conditions, meant to represent the physical properties of continents and oceans, respectively (Cooper, Moresi & Lenardic 2013; Ripesi *et al.* 2014; Wang, Huang & Xia 2017; Bakhuis *et al.* 2018). However, the experimental and numerical results for this configuration appear to be at odds with each other (Ostilla-Mónico 2017).

Studies of RB with mixed-temperature boundary conditions were pioneered by the simulations of Cooper *et al.* (2013), who studied the effect of large or small patches of adiabatic 'continents' in a doubly periodic, large-aspect-ratio RB simulation domain (cell). Cooper *et al.* (2013) found that the heat transfer was largely unaffected by the number of continental blocks, and depended on area coverage. These results were corroborated experimentally by Wang *et al.* (2017), who found that the heat transfer in their rectangular RB cell depended mainly on the conducting area, and was largely independent of the arrangement of the plates. For both studies, the arrangement of the plates had a substantial effect on the underlying flow. The role of plate size and shape was postulated to be crucial in understanding the role continental and oceanic plates play in the configuration of the mantle circulation, and how these interactions determine the dynamics of the Wilson cycle (Ostilla-Mónico 2017).

Conversely, the simulations of Ripesi *et al.* (2014) in two dimensions, and their recent extension by Bakhuis *et al.* (2018) to three dimensions, focused on patches which have characteristic dimensions smaller than the distance between the plates. These simulations found that the arrangement of the plates, quantified as a stripe wavelength, had a substantial effect on the total heat transport, and that once the stripe wavelength became comparable to the size of the thermal boundary layer, the heat transport asymptotically reached the values corresponding to a fully conducting plate, even if the conducting area was only one-half. But unlike the studies mentioned above, both of these studies found that plate size had no significant effect on the flow dynamics.

The discrepancy between these two results becomes less apparent when one compares the wavelengths of the inhomogeneities. The stripes in the first case scenario, by Cooper *et al.* (2013) and Wang *et al.* (2017), are much larger than the stripes in the second case scenario, by Ripesi *et al.* (2014) and Bakhuis *et al.* (2018). This discrepancy just indicates that there are two distinct regimes, and that a crossover between the two regimes must exist: between large adiabatic patches which significantly affect the flow topology and small adiabatic patches whose effect is only present very close to the plates, there must be a transitional regime with 'medium-sized' patches which affect both types of statistics. Because land masses such as continents and islands come in a wide variety of shapes and length-scales, understanding how these sizes and shapes affect the circulation of the mantle can enhance our understanding of continental drift.

In this study we set out to find the location and characteristics of the crossover regime between the 'large' and 'small' pattern behaviour, and to explore its characteristics through three-dimensional direct numerical simulations. For this, we will simulate three-dimensional RB with non-uniform temperature boundary conditions on the top surface, which are a mixture of adiabatic and perfectly conducting. We note that this transition might not happen at the same stripe size for different statistics, as has been seen for example in the transition between different flow regimes in rotating RB convection (Kunnen *et al.* 2016).

https://doi.org/10.1017/jfm.2020.623 Published online by Cambridge University Press

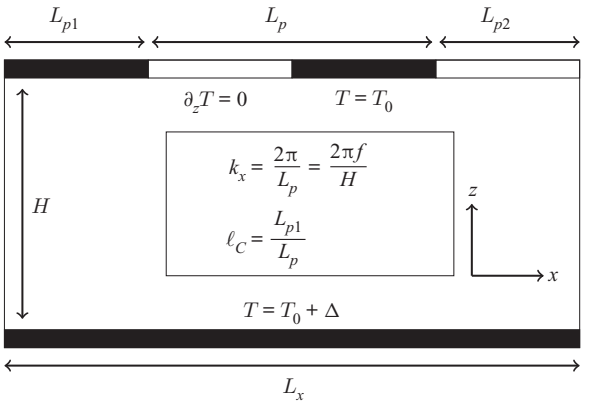


FIGURE 1. Schematic of the simulation set-up. The third dimension is removed for clarity purposes. The bottom plate is set at a constant (hot) temperature, while in the top plate, stripes of adiabatic and conducting boundary conditions alternate every L_p. We set $L_{p1} = L_{p2}$ so that the effective area of conducting material is 50 %.

2. Numerical details

We perform large-aspect-ratio simulations of RB flow using a second-order, centred finite difference code (van der Poel *et al.* 2015). The code is periodic in the wall-parallel directions with equal periodicity lengths of $L_x = L_y = L$. We fix the Rayleigh number to $Ra = g\beta\Delta H^3/(\nu\kappa) = 10^8$, and vary the Prandtl number $Pr = \nu/\kappa$ between 1 and 100, where g is the acceleration of gravity, β is the fluid thermal expansion coefficient, Δ is the hot-cold temperature difference, H is the height of the cell, and ν and κ are the kinematic viscosity and thermal diffusivity of the fluid. The temperature boundary conditions are imposed as Dirichlet boundary conditions on the conducting parts of the plates: the bottom plate is fixed to a temperature Δ above that of the conducting regions of the top plate. In this way, the Rayleigh number Ra can be thought of as a non-dimensional measure of the temperature difference while the Prandtl number is a fluid property. The two-dimensional adiabatic stripes are introduced in the top plate using Neumann no-flux conditions. This means that the temperature of the fluid close to the adiabatic plates is not determined *a priori*. See figure 1 for a sketch of the configuration and figure 2 for a flow visualization.

The non-dimensionalized periodicity of the system, $\Gamma = L/H$, is a numerical parameter whose influence we want to remove as much as possible. We simulate aspect ratios in the range from $\Gamma = L/H = 1$ to $\Gamma = 16$. Previous studies (Stevens *et al.* 2018) have shown that it has a strong influence on the underlying statistics of the flow. As we will discuss further below, an adequately normalized heat transfer, as studied by Bakhuis *et al.* (2018), does not show significant box-size/domain-size dependence. The temperature statistics show some box-size dependence, especially when the number of unit patterns in the domain is small. The velocity statistics show a strong box-size dependence, which increases with Prandtl number. For $Pr = 1$, the velocity statistics for the two horizontal directions are approximately equal when $\Gamma \gtrsim 2$. But for $Pr = 100$, even at $\Gamma = 8$ we could not recover isotropic statistics in both horizontal directions. Therefore, velocity statistics will only be shown for $Pr = 1$, where we can be sure that any anisotropy between the horizontal directions is produced by the inhomogeneous boundary conditions instead of by numerical effects.

https://doi.org/10.1017/jfm.2020.623 Published online by Cambridge University Press

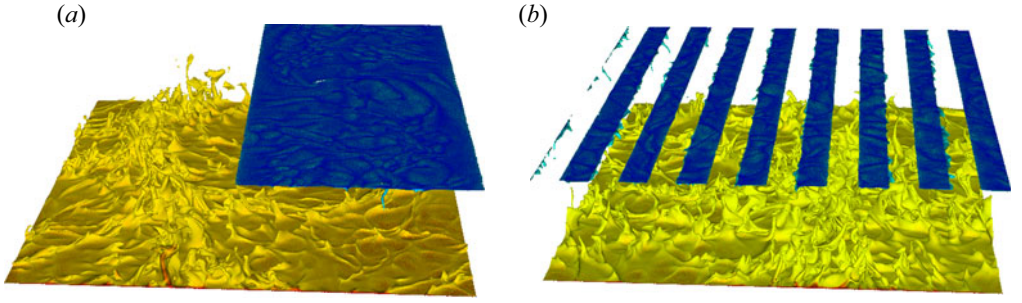


FIGURE 2. Volume rendering visualization of the instantaneous temperature for two cases simulated at $Ra = 10^8$, $Pr = 1$ and $\Gamma = 4$. Red denotes hot fluid while blue denotes cold fluid. (*a*) Large stripes with $f = 0.25$. The stripes cause a substantial ordering of the plume dynamics in the bottom plate, and an overall increase in temperature. (*b*) Small stripes with $f = 2$. The stripes do not affect the flow dynamics at the bottom plate.

Γ	f
1	1, 2, 4, 6, 10, 15, 20, 30, 45, 60, 90
2	0.5, 1, 2, 4, 10
4	0.25, 0.5, 1, 2, 4
8	0.125, 0.25, 0.5
16	0.125 (Only $Pr = 1$)

TABLE 1. Simulated values of f and Γ.

To fully capture the crossover regime, we simulate a wide range of stripe wavenumbers $k_x = 2\pi/L_p$, where $L_p = H/f$ is the stripe wavelength, and f is the number of stripes per unit non-dimensional length (non-dimensionalized using the height). We set $L_{p1} = L_{p2}$, and keep the top plate equally partitioned between conducting and adiabatic regions. The largest wavelength covered is $f = 1/8$, representing a single stripe pair in a $\Gamma = 8$ domain. This wavelength is larger than that in the experiments by Wang *et al.* (2017), and will cover the full experimental parameter regime. The smallest wavelength is $f = 90$, well into the asymptotic small-patch region according to Bakhuis *et al.* (2018). Due to the second-order scheme of the code used, each stripe must be resolved by at least four points; otherwise artefacts are introduced. This means that to keep on increasing f, we would have to increase the resolution. Because of this, we limited ourselves to $f \leq 90$. Furthermore, we note that for some values of f, we have simulated several periodicity aspect ratios Γ to quantify the domain independence. A full list of all the simulated Γ and f is available in table 1.

We will focus on one-dimensional stripes on the plates, as our previous exploration of chequerboard patterns showed that they do not produce significantly different physics (Bakhuis *et al.* 2018). However, stripes introduce an asymmetry between the two horizontal directions which can affect the flow enhancement. We have also simulated two cases with chequerboard inhomogeneities to better quantify the effects of boundary asymmetry against large, but isotropic, inhomogeneities.

The grid resolution used for this study conforms to the grid convergence study performed by Bakhuis *et al.* (2018) for $Pr = 1$. For larger Prandtl numbers, we use the same resolution, and check its adequacy by monitoring the balance between viscous

https://doi.org/10.1017/jfm.2020.623 Published online by Cambridge University Press

dissipation and heat transport outlined in Stevens, Verzicco & Lohse (2010). Finally, temporal convergence is assessed through measuring the non-dimensional heat transport, i.e. the Nusselt number $Nu = Q/(\kappa \Delta H^{-1})$, with Q the plate-to-plate heat transfer. While Q can be measured in many ways (Shraiman & Siggia 1990), we use the volumetrically and temporally averaged value of $\langle u_z \theta \rangle$ to obtain the numerical value of Q. As this is a second-order correlation, which takes longer to converge, it provides some bounds on our temporal convergence errors. We have run the simulations for small domains with $\Gamma = 1$ up to 1200 large-eddy turnover times, and for larger domains with $\Gamma = 8$ up to 120 large-eddy turnover times. This gives us an error bound on temporal convergence of less than 1 %.

3. Results

We start by showing a visualization of the instantaneous temperature field for two cases with different values of f in figure 2. From a cursory glance, we can confirm what was detailed in the introduction: two very different regimes exist, one where the stripes are small and the flow dynamics is not significantly affected as compared to the case of a fully conducting top plate (shown on the right), and one where the stripes are large and the flow dynamics is substantially changed due to the presence of a large adiabatic surface on only one side (shown on the left). The rest of this manuscript will involve teasing out the differences between the two flow regimes, when the transition between them happens, and how these differences affect the flow statistics.

3.1. *Heat transfer*

We first focus on the heat transfer, non-dimensionalized as a Nusselt number Nu. The first step is to eliminate box-size dependence Γ, so that $Nu(f)$ can be properly elucidated. As mentioned previously, we have conducted simulations for different aspect ratios Γ with all other control parameters constant, to quantify as far as possible this dependence. Figure 3(a) shows the Nusselt number $Nu(\Gamma, f)$ against stripe frequency for $Pr = 1$. The box-size dependence of Nu can be appreciated in the fact that the data points for the same values of f do not fall onto each other when Γ is changed. This is not surprising, because from RB simulations with homogeneous boundary conditions, it is known that for $Pr = 1$, the Nusselt number shows some box-size dependence if $\Gamma \leq 4$ (Stevens *et al.* 2018). This dependence is further quantified in panel (d), where the Nusselt number of the fully conducting (unmodified) system is shown as a function of Γ. While the variations are not very large, of the order of 6 %, they are enough to introduce discrepancies into the measurements.

The Γ dependence can be removed by adequately compensating Nu. In figure 3(b), we plot the normalized Nusselt number $Nu/Nu_{fc}(\Gamma)$, where $Nu_{fc}(\Gamma)$ is the Nusselt number for the homogeneous (fully conducting plates) case from the panel (c). With this operation, we get an excellent collapse across all box sizes, removing the Γ dependence and elucidating the dependence on f. For values of f less than 1, the heat transport is almost constant, and independent of stripe wavelength. This is consistent with the observations by Cooper *et al.* (2013) and Wang *et al.* (2017). For values of f greater than 1, the heat transport begins to significantly increase, and tends towards the fully conducting value, which is consistent with Bakhuis *et al.* (2018).

For our simulations we are not able to reach $Nu/Nu_{fc} = 1$ because we are limited in the values of f we can simulate. This asymptotic value for Nu/Nu_{fc} was reached in Bakhuis

https://doi.org/10.1017/jfm.2020.623 Published online by Cambridge University Press

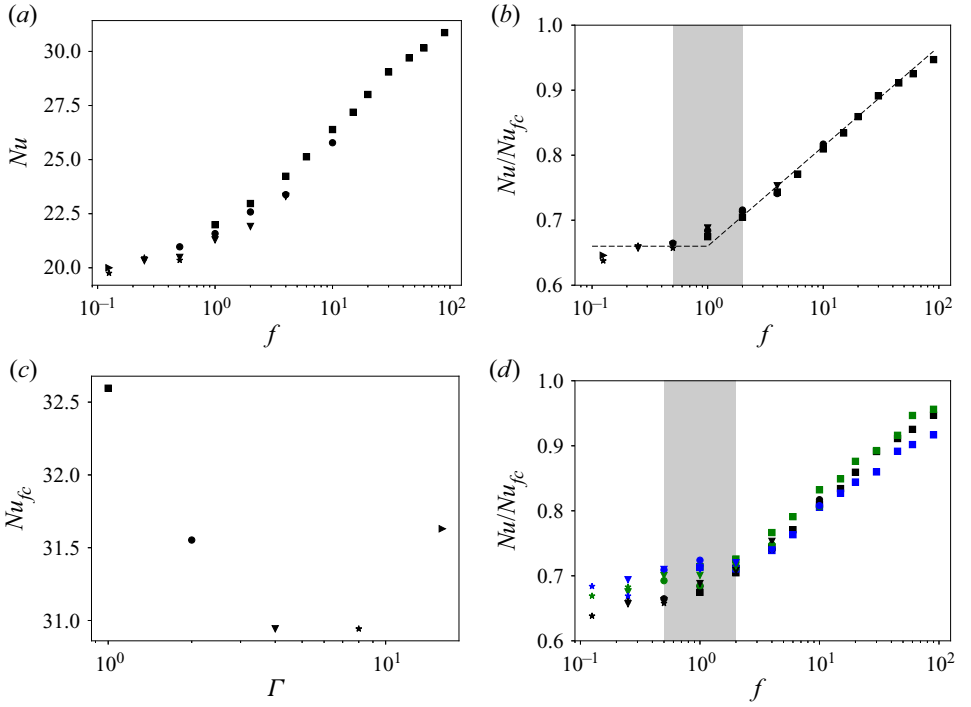


FIGURE 3. (*a*) Nusselt number against stripe number for $Ra = 10^8$ and $Pr = 1$. A large variation between different values of Γ can be seen. (*c*) Nusselt number variation as a function of box size for $Pr = 1$. (*b*) Normalized Nusselt number for $Pr = 1$. The box-size dependence is removed when normalizing by a Γ-dependent fully conducting Nu_{fc}. (*d*) Nusselt number normalized by the fully conducting value for each value of Γ. A large degree of collapse can be found across Pr. Symbols: colour denotes Prandtl number; $Pr = 1$ is black, $Pr = 10$ is green and $Pr = 100$ is blue. Shape denotes Γ; squares are $\Gamma = 1$, circles are $\Gamma = 2$, V-triangles are $\Gamma = 4$, stars are $\Gamma = 8$ and $>$-triangles are $\Gamma = 16$.

et al. (2018) at lower Rayleigh numbers. For this to happen, the pattern size has to be much smaller than the thermal boundary layer size, implying notably finer grid resolution. If we estimate the thermal boundary layer size as $\lambda_T/H = 1/(2Nu)$, this gives us the requirement of $f \gg 2Nu$ for $Nu/Nu_{fc} \to 1$. With our current Rayleigh number $Ra = 10^8$, this should happen for $f \gg 65$. The largest value of f simulated, $f = 90$, is insufficient to see this.

In figure 3(*b*), we also shade in a postulated transitional region $0.5 < f < 2$ between the two regimes. None of the aforementioned studies examined values on both sides of $f = 1$, i.e. they did not explore the transitional region between the two behaviours, so they unsurprisingly reached different conclusions on the behaviour of the heat transport.

We attempt to extend this result for all Prandtl numbers simulated in figure 3(*d*), which shows the normalized Nusselt number for three different Prandtl numbers. While the basic result remains, i.e. there is a sharp transition between two regimes of heat transport, the behaviour on both regimes appears slightly different. At first glance, the low-wavelength limit values of Nu/Nu_{fc} are higher with increasing Pr, but it remains to be seen if these values would continue dropping as f decreases, or if this is a product of the increased box-size dependence seen for larger Prandtl numbers (Stevens *et al.* 2018). The slope of the $Nu/Nu_{fc}(f)$ relationship also appears to be steeper for higher Pr. The mechanisms for

https://doi.org/10.1017/jfm.2020.623 Published online by Cambridge University Press

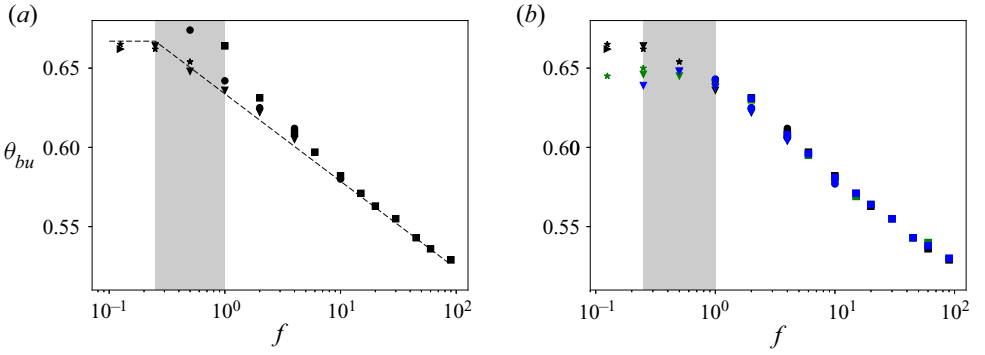


FIGURE 4. (*a*) Mid-gap temperature as a function of f for $Pr = 1$ and all box sizes simulated. The box-size dependence of some simulations is emphasized. (*b*) Mid-gap temperature as a function of f for all Pr simulated and selected box sizes. A clear transition between a constant-temperature region and a region of decreasing bulk-temperature can be seen. Shapes and colours of symbols are the same as in figure 3.

this are unclear, and any speculation on these trends is out of the scope of this study. What appears to be a general conclusion is that the wide-stripe and thin-stripe regimes exist independently of Pr in our range of $1 \leq Pr \leq 100$, and we expect them to persist as the geophysically relevant regime $Pr \to \infty$ is entered.

3.2. *Temperature profiles*

The next thing we study is the dependence of the mean temperature at the mid-plane on the value of f. We do this by averaging the temperature in both horizontal directions, and in time (after the flow becomes statistically stationary). Bakhuis *et al.* (2018) concluded that as $f \to \infty$, the temperature in the mid-plane region would tend towards the arithmetic mean of the temperatures of the two plates, i.e. $\theta = 0.5$, and that as the stripes became larger ($f \to 0$), the mean temperature would tend towards $2/3$. This was rationalized by taking an average of the temperatures at the two plates, weighted by the fraction of the plate which actually conducted heat. For $\ell_C = 0.5$, this gives $\theta = 2/3$.

Figure 4(*a*) shows the average mid-gap temperature as a function of f for $Pr = 1$. In analysing the current simulations, it becomes clear that the simulations of Bakhuis *et al.* (2018) have significant box-size dependence in their temperature measurements, due to the enforced periodicity constraining the flow and the development of large-scale structures. There is a strong box-size dependence in the transitional region. When running a small periodic box with only one or two stripes per simulation period, the temperature tends to increase due to the finite domain size. Only when $\Gamma = 4$ or $\Gamma = 8$ are these effects mitigated, and we can obtain box-size-independent results for $f \leq 1$. As rationalized earlier, the mid-gap temperature can be seen to saturate to $\theta_{bu} = 2/3$ for $f \leq 0.25$, representing stripes of very large size. Consistent with Bakhuis *et al.* (2018), we see a sharp temperature drop as f increases beyond $f = 1$. We have shaded in a transitional region, which now happens for other values of f: $0.25 < f < 1$. To adequately capture this region, simulations of $\Gamma \geq 4$ are needed, which were not performed in Bakhuis *et al.* (2018).

In figure 4(*b*) we show the bulk temperature as a function of f for all the Prandtl numbers explored. Simulations which have a single unit pattern per box size are taken out of the

https://doi.org/10.1017/jfm.2020.623 Published online by Cambridge University Press

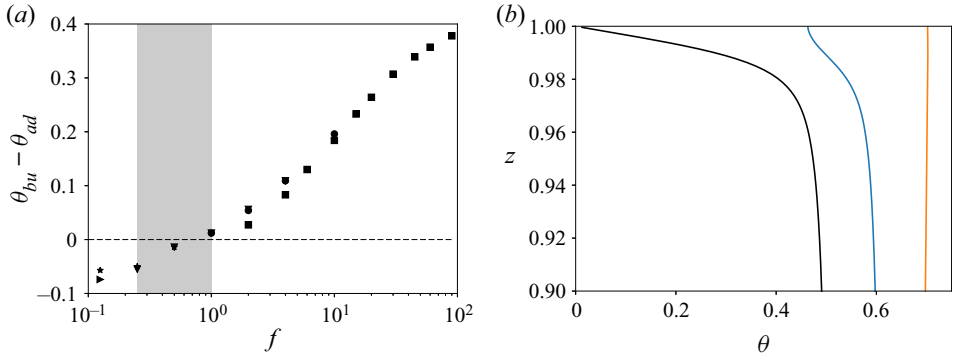


FIGURE 5. (*a*) Difference between the mid-gap temperature θ_{bu} and the average temperature of the fluid near the adiabatic plate as a function of f for $Pr = 1$ and all box sizes simulated. Shapes of symbols are the same as in figure 3. (*b*) Thermal boundary layer profiles close to the adiabatic plates for $\Gamma = 4$, $Pr = 1$ and $f = 4$ (blue), $f = 0.25$ (orange), and the reference (homogeneous) case (black).

results. By doing this, we see how the curves collapse in the high-f region. Again, there is a transitional region which happens for $0.25 < f < 1$. The values of f at which this transition happens are independent of Pr, but are different from (smaller than) those from the transition we saw in Nu/Nu_{fc}. Because of this, the low-f region appears decreased in size in the figure.

We can further explore the temperature statistics by analysing the behaviour of the average fluid temperature close to the adiabatic plates (θ_{ad}). Naively, we can expect the temperature of the adiabatic regions to tend towards the (cold) plate temperature $\theta = 0$ as f increases, and this is indeed what happens. What is more interesting is to look at the temperature difference between bulk and adiabatic region as a function of f, which we show in figure 5(*a*). For large f, the bulk is hotter than the adiabatic regions at the top, cold plate, as expected. However, for $f < 1$, the fluid close to the adiabatic regions becomes slightly hotter than the bulk fluid (as well as the conducting parts of the same plate), which means that there is a slight temperature inversion. This provides another statistic that shows a change in behaviour during the transition.

To further understand what is happening, we show the thermal boundary layer close to the adiabatic regions for a small-f and a large-f case in figure 5(*b*). For large f, we can see that inside the boundary layer, there is a temperature increase, which means that there is horizontal transport of heat to the conducting regions. For small f, this gradient is not seen, which means that the horizontal transport of heat within the boundary layers is severely weakened. This has the potential to generate strong horizontal flows due to strong density gradients, which we analyse in the next section.

3.3. *Velocity statistics and flow structure*

Finally, we analyse the velocity statistics and the changes in flow structure. As mentioned in the introduction, from the experimental and numerical results we expect that the large-stripe cases show a strong effect on the wind, while the small-stripe cases should not be very different from the canonical set-up. We could also expect to see a strong asymmetry in the winds once the stripes pass a certain size, as excess heat must be

https://doi.org/10.1017/jfm.2020.623 Published online by Cambridge University Press

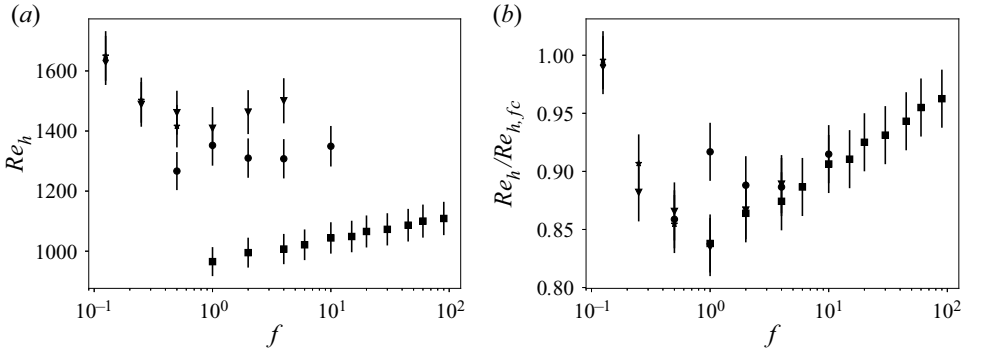


FIGURE 6. (*a*) Total horizontal flow strength quantified as a Reynolds number. (*b*) Total horizontal flow strength normalized by the homogeneous case. Symbol shapes are as in figure 3. Error bars of 5 % are included on both plots.

redistributed horizontally from the zones close to adiabatic boundary conditions to the cooling parts of the plate.

To study the velocity statistics, we define the 'wind' Reynolds number in the ith direction as $Re_i = u_i' H/\nu$, where u' is the volume-averaged root-mean-square velocity. We also define the horizontal wind Reynolds number as $Re_h = \sqrt{Re_x^2 + Re_y^2}$. For the homogeneous case, u_x' should be equal to u_y', meaning $Re_x = Re_y$. This means that Re_h should be equal to $\sqrt{2}Re_x$, which is also equal to $\sqrt{2}Re_y$. However, because of the restrictions present due to the finite domain (i.e. finite Γ), Re_x and Re_y often differ from each other. Of all the statistics presented in this manuscript, Re has the largest box-size dependence. This is true even for the case of fully conducting plates, as was shown by Stevens *et al.* (2018). For $Pr = 1$, Re_x and Re_y differ from each other by about 5 %, which gives us an estimate of the error made when measuring these quantities. For $Pr = 10$ and $Pr = 100$, the anisotropy is stronger, and causes deviations between Re_x and Re_y of over 100 %. This means our error bars become too large to extract any meaningful information. Because of this, in this section we only show results for $Pr = 1$.

In figure 6(*a*), we show the horizontal Reynolds number Re_h as a function of f for the different values of Γ. The dependence of Re_h on Γ is very strong: when comparing the values of Re_h for the $f = 10$ case at $\Gamma = 1$ against the same f at $\Gamma = 2$, Re_h can be seen to be as much as twice as large for $\Gamma = 2$. When looking at both horizontal directions together, the underlying flow appears weaker than in the homogeneous case. This is further quantified in panel (*b*), where we show Re_h normalized by the fully conducting value $Re_{h,fc}$, which is Γ-dependent. From the figure we can observe a local minimum for Re_h around $f = 1$. As $f \to \infty$, we recover the homogeneous Re_h, and as f becomes smaller than unity, the wind is enhanced by strong horizontal temperature gradients. For no cases simulated does the total wind strength exceed that of the homogeneous flow even if the data hint that this will happen for $f < 0.1$.

We now turn to the behaviour of the individual Re_i as a function of the stripe wavelength, which is illustrated in figure 7; here we expect to see differences between the x and y directions due to the asymmetry introduced by the stripes. In figure 7(*a*), we show the large variability between the different values of Re_x and Re_y for different box sizes and different values of f. We can highlight two trends. First, for large stripes ($f < 1$), the wind in the direction normal to the stripes, i.e. the x direction, is much larger than the wind in

https://doi.org/10.1017/jfm.2020.623 Published online by Cambridge University Press

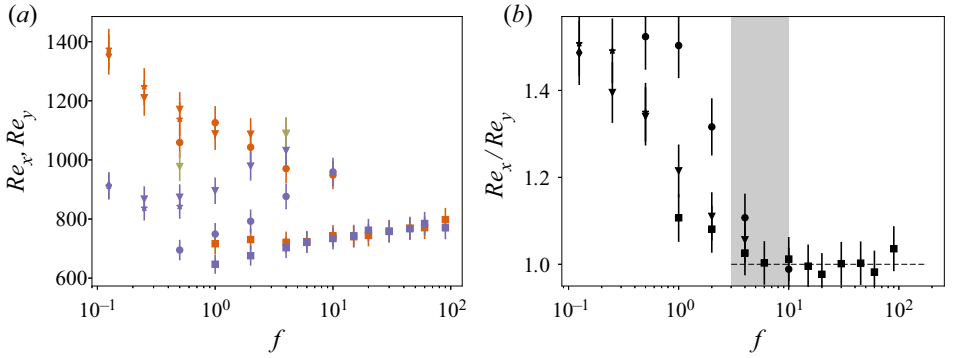


FIGURE 7. (*a*) Flow strength quantified as a Reynolds number in the stripe-normal (Re_x, orange symbols) and stripe-parallel (Re_y, purple symbols) directions. Data for the average horizontal Reynolds number ($[Re_x + Re_y]/2$) for the chequerboard pattern simulations are included in khaki. (*b*) Ratio between the wind Reynolds numbers in the horizontal directions. Symbol shapes are as in figure 3. Error bars of 5 % are included on both plots. Only data for $Pr = 1$ are presented here.

the direction parallel to the stripes, i.e. the y direction. As the stripes become smaller, the winds tend to equalize. In the direction parallel to the stripes, the wind increases, while in the direction perpendicular to the stripes, the wind decreases. This is further quantified in figure 7(*b*), which shows the ratio between Re_x and Re_y. Once the stripes are small enough, around $f = 4$, the two Reynolds numbers become approximately equal, but they still are somewhat lower than the value for fully conducting plates, which is not reached until f becomes much higher.

This asymmetric wind increase appears regardless of box size, even if there is some scatter on the magnitude of the asymmetry depending on Γ. Again, we have highlighted the transitional region where the asymmetry disappears, which now occurs for higher values of f: $3 < f < 8$. We emphasize that the transitional ranges for the three statistics happen for different values of f, even if they are generally around $f = 1$.

We have also simulated two cases with a chequerboard pattern. This pattern restores the x–y asymmetry, and serves to quantify how much of the wind enhancement comes from the necessity of transporting heat to the regions where it can be cooled by the plates instead of from the asymmetry of the system. The chequerboard cases were run for $\Gamma = 4$ with $f = 0.5$ and $f = 4$. Unsurprisingly, we find that $Re_x \approx Re_y$ to within 5 %, the previously reported error bound. What is more interesting is to compare the flow strength to the other case. This shows that the wind enhancement disappears with the flow asymmetry: for $f = 0.5$ the value of the horizontal Reynolds number is lower than that for $f = 16$, and this one is slightly below that of the homogeneous case. It is only when there is a strong asymmetry in the horizontal directions that intense large-scale flow patterns are generated in the direction perpendicular to the stripes, and the wind can exceed the value of the homogeneous case in a single direction.

As discussed in § 2 we only include results for $Pr = 1$. For $Pr = 10$ and $Pr = 100$, a similar enhancement of the flow strength and anisotropy could be seen when applying the stripe pattern, but we cannot confidently attribute it to physical reasons alone. For this reason we decided not to show these data. Further studies at increasing box size at high Pr are required to adequately disentangle the box-size effects from those coming from inhomogeneous boundary conditions.

https://doi.org/10.1017/jfm.2020.623 Published online by Cambridge University Press

4. Conclusions

We have conducted numerical simulations of adiabatic–conducting stripe pairs of RB flow in an attempt to uncover the differences between the large-stripe regime of Cooper *et al.* (2013) and Wang *et al.* (2017) and the small-stripe regime of Ripesi *et al.* (2014) and Bakhuis *et al.* (2018). We observed that for $Ra = 10^8$ and $Pr > 1$, a transition between the two behaviours happens at around $f = 1$, that is, with stripes the size of the plate distance. We note that the statistics show transitions at different values of f, and that these transitions can only be fully uncovered once the simulation 'box size' is large enough, but as a rule of thumb, they happen around $f \approx 1$. While this is not totally satisfactory, we point out that for rotating RB, we have previously seen that different statistics, such as fluctuations or mean temperature profiles, have different transition points (Kunnen *et al.* 2016).

The small-stripe regime is characterized by a heat transport that is very dependent on stripe wavelength. With decreasing stripe wavelength, the bulk temperature and heat transport asymptotically tend to the fully conducting values, even when only half the plate is conducting. This regime was already explored in detail by Bakhuis *et al.* (2018). Only when the stripes become very small, i.e. $f \gg 2Nu$, do the statistics converge to those of fully conducting plates.

The large-stripe regime is characterized by a heat transport and a bulk temperature that is independent of stripe wavelength. To maintain the heat transport as the stripes become large, the underlying flow is heavily modified (as observed by Wang *et al.* 2017) and the velocities in the stripe-normal direction increase substantially with increasing stripe length. The temperature stabilizes at values around $2/3$, i.e. the weighted average of the plate temperatures, but this appears to depend on Prandtl number. There appears to be a local temperature inversion, where the temperature at the adiabatic plates is higher than the bulk temperature. This regime is geophysically interesting, as many variations on the RB problem, such as mantle convection, consist of very long wavelength inhomogeneities. We confirm here that these types of variations can lead to the enhancement of underlying 'winds' or circulations.

However, the conclusions here are limited in two main ways. The simulation of large-Pr flows is complicated due to the resolution requirements and the computational box sizes. The effect of Pr on enhancing winds has to be quantified in a more detailed manner. In the second place, the value of l_C, i.e. the ratio of conducting to adiabatic areas, has been fixed at one-half. Repeating this study for other values of l_C is necessary to achieve more robust conclusions.

Acknowledgements

We thank A. Blass, D. Bakhuis and R. J. A. M. Stevens for providing their data. We thank the HPE Data Science Institute (HPE DSI) at the University of Houston for providing computing resources.

Declaration of interests

The authors report no conflict of interest.

REFERENCES

AHLERS, G., GROSSMANN, S. & LOHSE, D. 2009 Heat transfer and large scale dynamics in turbulent Rayleigh–Bénard convection. *Rev. Mod. Phys.* **81**, 503.

https://doi.org/10.1017/jfm.2020.623 Published online by Cambridge University Press

BAKHUIS, D., OSTILLA-MÓNICO, R., VAN DER POEL, E. P., VERZICCO, R. & LOHSE, D. 2018 Mixed insulating and conducting thermal boundary conditions in Rayleigh–Bénard convection. *J. Fluid Mech.* **835**, 491–511.

BROWN, E., FUNFSCHILLING, D., NIKOLAENKO, A. & AHLERS, G. 2005 Heat transport by turbulent Rayleigh–Bénard convection: effect of finite top- and bottom conductivity. *Phys. Fluids* **17**, 075108.

CHILLÀ, F. & SCHUMACHER, J. 2012 New perspectives in turbulent Rayleigh–Bénard convection. *Eur. Phys. J.* E **35** (7), 58.

COOPER, C. M., MORESI, L.-N. & LENARDIC, A. 2013 Effects of continental configuration on mantle heat loss. *Geophys. Res. Lett.* **40** (11), 2647–2651.

KUNNEN, R. P. J., OSTILLA-MÓNICO, R, VAN DER POEL, E. P., VERZICCO, R. & LOHSE, D. 2016 Transition to geostrophic convection: the role of the boundary conditions. *J. Fluid Mech.* **799**, 413–432.

LENARDIC, A & MORESI, L 2003 Thermal convection below a conducting lid of variable extent: heat flow scalings and two-dimensional, infinite Prandtl number numerical simulations. *Phys. Fluids* **15** (2), 455–466.

LENARDIC, A., MORESI, L.-N., JELLINEK, A. M. & MANGA, M. 2005 Continental insulation, mantle cooling, and the surface area of oceans and continents. *Earth Planet. Sci. Lett.* **234** (3–4), 317–333.

LOHSE, D. & XIA, K.-Q. 2010 Small-scale properties of turbulent Rayleigh–Bénard convection. *Ann. Rev. Fluid Mech.* **42**, 335–364.

OSTILLA-MÓNICO, R. 2017 Mixed thermal conditions in convection: how do continents affect the mantle's circulation? *J. Fluid Mech.* **822**, 1–4.

PEKERIS, C. L. 1935 Thermal convection in the interior of the earth. *Geophys. J. Intl* **3**, 343–367.

VAN DER POEL, E. P., OSTILLA-MONICO, R., DONNERS, J. & VERZICCO, R. 2015 A pencil distributed finite difference code for strongly turbulent wall-bounded flows. *Comput. Fluids* **116**, 10–16.

VAN DER POEL, E. P., OSTILLA-MÓNICO, R., VERZICCO, R. & LOHSE, D. 2014 Effect of velocity boundary conditions on the heat transfer and flow topology in two-dimensional Rayleigh–Bénard convection. *Phys. Rev.* E **90**, 013017.

RIPESI, P., BIFERALE, L., SBRAGAGLIA, M. & WIRTH, A. 2014 Natural convection with mixed insulating and conducting boundary conditions: low- and high-Rayleigh-number regimes. *J. Fluid Mech.* **742**, 636–663.

RUSAOUËN, E., LIOT, O., CASTAING, B., SALORT, J. & CHILLÀ, F. 2018 Thermal transfer in Rayleigh–Bénard cell with smooth or rough boundaries. *J. Fluid Mech.* **837**, 443–460.

SHRAIMAN, B. I. & SIGGIA, E. D. 1990 Heat transport in high-Rayleigh number convection. *Phys. Rev.* A **42**, 3650–3653.

SOLOMATOV, V. S. & MORESI, L.-N. 2000 Scaling of time-dependent stagnant lid convection: application to small-scale convection on earth and other terrestrial planets. *J. Geophys. Res.* **105** (B9), 21795–21817.

STEVENS, R. J. A. M., BLASS, A., ZHU, X., VERZICCO, R. & LOHSE, D. 2018 Turbulent thermal superstructures in Rayleigh–Bénard convection. *Phys. Rev. Fluids* **3** (4), 041501.

STEVENS, R. J. A. M., VERZICCO, R. & LOHSE, D. 2010 Radial boundary layer structure and Nusselt number in Rayleigh–Bénard convection. *J. Fluid Mech.* **643**, 495–507.

TISSERAND, J. C., CREYSSELS, M., GASTEUIL, Y., PABIOU, H., GIBERT, M., CASTATING, B. & CHILLA, F. 2011 Comparison between rough and smooth plates within the same Rayleigh–Bénard cell. *Phys. Fluids* **23**, 015105.

VERZICCO, R. 2004 Effect of non-perfect thermal sources in turbulent thermal convection. *Phys. Fluids* **16**, 1965–1979.

WANG, F., HUANG, S.-D. & XIA, K.-Q. 2017 Thermal convection with mixed thermal boundary conditions: effects of insulating lids at the top. *J. Fluid Mech.* **817**, R1.

XIA, K.-Q. & LUI, S.-L. 1997 Turbulent thermal convection with an obstructed sidewall. *Phys. Rev. Lett.* **79**, 5006–5009.

https://doi.org/10.1017/jfm.2020.623 Published online by Cambridge University Press